Injection intensity-dependent recombination at various grain boundary types in multicrystalline silicon solar cells

[1]F. Frühauf, [2]P.P. Altermatt, [3]T. Luka, [4]T. Mehl, [1]H. Deniz, and [1]O. Breitenstein*

[1]Max Planck Institute of Microstructure Physics, Halle, Germany

[2]Global Photovoltaic Simulation Group, Case Postale 1056, 1211 Genève 1, Switzerland

[3]Fraunhofer Center for Silicon Photovoltaics (CSP), Halle, Germany

[4]Norwegian University of Life Sciences, Ås, Norway

*Corresponding author, E-Mail: breiten@mpi-halle.mpg.de

Keywords: Photoluminescence imaging, light beam-induced current, device simulation, injection-dependent recombination

Abstract

If the ratio of two open circuit photoluminescence (V_{oc}-PL) images taken at two different light intensities is displayed, some grain boundaries (GBs) may show up as bright lines. This indicates that these special GBs show distinct injection intensity-dependent recombination properties. It will be shown here that this results in an apparent ideality factor of the light emission smaller than unity. The effect is reproduced with numerical device simulations using a usual distribution of defects in the band gap along grain boundaries. Quantitative imaging of this apparent luminescence ideality factor by PL imaging is complicated by the lateral horizontal balancing currents flowing at open circuit. The local voltage response of an inhomogeneous solar cell at different injection levels under open circuit is modelled by Griddler simulations, based on PL investigations of this cell. The evaluation of V_{oc}-PL images at different illumination intensities allows us to conclude that the apparent luminescence ideality factor at the special GBs is about 0.89, whereas in the other regions it is between 0.94 and 0.95. Reverse bias electroluminescence showed no pre-breakdown sites, and hyperspectral PL imaging showed only in one of the investigated GBs particular defect luminescence. TEM investigations of two GBs, one showing distinct injection intensity-dependent recombination and the other one showing none, revealed that the investigated special GB is a large-angle GB whereas the GB not showing this effect is a small-angle GB.

1. Introduction

Electroluminescence (EL) and photoluminescence (PL) imaging are standard tools to study local electronic properties of solar cells. This holds in particular for cells made from multicrystalline (mc) silicon material, which still represent the major part of all solar cells produced today. Therefore a comprehensive study of the electronic properties of the extended crystal defects in mc-Si material and cells is necessary, since these defects are governing the energy conversion losses in these cells. Grain boundaries (GBs) and dislocation networks represent the significant contribution to these extended defects. It is well-known that different types of GBs in mc-Si show different recombination properties. For example, twins on (111) planes usually show little or no recombination activity, whereas low-angle GBs may show a high recombination activity [1]. These low-angle GBs are basically rows of dislocations. It was shown recently that, even within one and the same low-angle GB, regions of different recombination activity may exist, which differ in their type of dislocations representing the GB [2].

In this contribution we show by evaluating PL images of mc-Si solar cells that different GBs may show different degrees of injection intensity-dependent recombination activity. It will be shown by a simplified analytic analysis that this property can be described by an apparent ideality factor of the luminescence n_{lum} smaller than unity, which corresponds to a bulk recombination current ideality factor n_1 larger than unity. The effect is reproduced with numerical device simulations using a usual distribution of defects in the band gap along grain boundaries. In principle, n_{lum} can be imaged by evaluating V_{oc}-PL images taken at different illumination intensities. The difference between the applied bias and the local diode voltages due to horizontal balancing currents may be regarded at least approximately by applying a recently introduced correction method evaluating V_{oc}-PL images at two illumination intensities [3]. In this work this correction method is extended to the evaluation of images taken at 4 different intensities. Based on this knowledge and on 2-dimensional finite element simulations of the cell using an independently measured J_{01} distribution, n_{lum} of the special GBs are measured. By transmission electron microscopy (TEM) the crystallographic structure of one of these GBs showing and one GB not showing injection-dependent recombination was determined. It was checked by reverse bias electroluminescence (ReBEL) [4] and hyperspectral PL imaging [5] whether these special GBs show particular defect luminescence.

2. Photoluminescence results

Two cells from different producers were investigated here, both being industrial standard technology Al-BSF (full-area back surface field) type multicrystalline (mc) cells with 3 busbars, 156x156 mm^2 in size. It should be noted that the special GBs reported here have been found also on several other cells of this type, hence they seem to be quite common at least in this type of solar cells. PL measurements have been performed under open circuit and short circuit conditions by using a custom built PL system employing LED illumination at 850 nm (870 nm short-pass filtered) and 950 to 1000 nm bandpass filtering in front of the thermoelectric-cooled ANDOR iKon-M PV-Inspector camera used with a LINOS inspec.x M NIR 1.4/50mm objective. All open circuit (V_{oc})-PL images shown and evaluated here are net PL images, hence from all of them a short circuit (J_{sc})-PL image taken at the same illumination intensity and acquisition time was subtracted, see [6]. This procedure makes the PL images equivalent to EL images for the same local diode voltage [7] and corrects for the baseline and residuals of the excitation illumination. For (V_{oc})-PL images the luminescence correction is very minor, but the baseline and illumination light correction remains important. Usually deconvolution of the luminescence images is applied for correcting photon scatter in the

detector [8,9]. We have shown recently [10] that, for our band-pass filtered luminescence images, deconvolution leads to minor improvements of the spatial resolution but may degrade the signal-to-noise ratio. Therefore we have not applied spatial deconvolution for most of our results. Only the final result of the image of the luminescence ideality factor will be presented either without or including spatial deconvolution of the luminescence images.

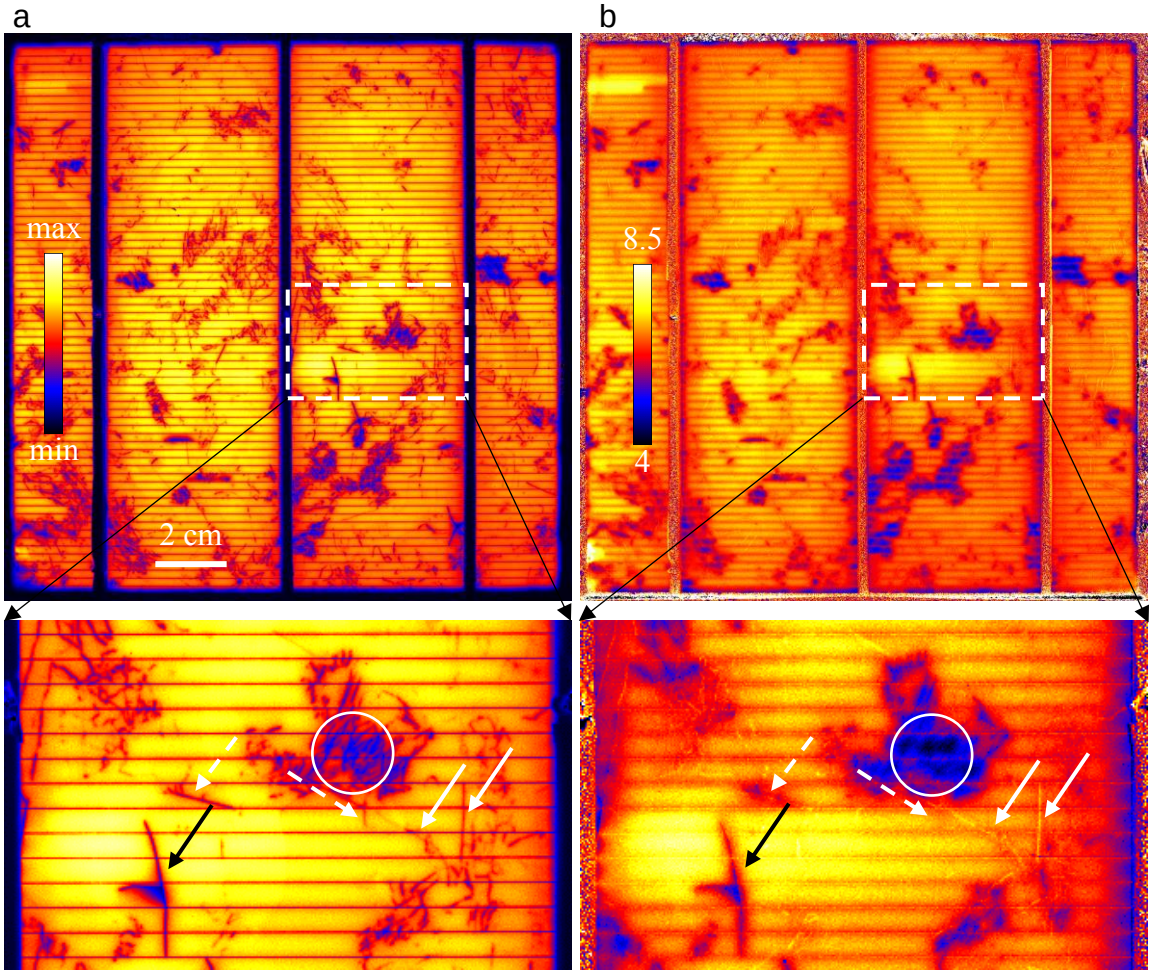

Fig. 1: a) V_{oc}-PL image of the first investigated cell at 0.5 sun [colors in a.u.], b) ratio of V_{oc}-PL images at 0.5 and at 0.1 suns intensity.

Fig. 1 a) shows a net V_{oc}-PL image of the first investigated cell taken at 0.5 sun equivalent intensity (measured by the nominal I_{sc}) together with an enlarged insert below. The same images measured at 0.1 sun intensity looked visually very similar. However, when the ratio of the 0.5 to the 0.1 suns images is displayed in Fig. 1 b), some bright lines appear in the enlarged insert, see white arrows. These lines are in the locations of certain isolated lying recombination-active grain boundaries, which look in a) very similar to other grain boundaries. In the ratio image (Fig. 1 b) other separately lying grain boundaries become invisible, see e.g. dashed white arrows. These GBs obviously show an injection-independent recombination. Some cracks in

the lower left of the enlarged region (black arrows) and all regions of a high local density of GBs, which may be considered as extended regions with increased recombination, appear dark in the ratio image b), see circle. This is an effect of the lateral series resistance as will be modelled in the next Section. Note that under V_{oc} condition, in defect regions of high bulk recombination current density J_{01}, the dark current dominates, whereas in "good" regions the photocurrent dominates. This leads to lateral balancing currents and thus to lateral diode voltage differences. In defect regions the local diode voltage is always smaller than in good cell regions, and these differences increase with increasing illumination intensity (linear response principle, see [17]). Therefore in these defect regions the local voltage is reduced more strongly at 0.5 suns than at 0.1 suns, leading to the dark contrast in these regions in the ratio image Fig. 1 b).

3. The apparent ideality factor of light emission

3.1. General considerations

It is well-known that Shockley-Read-Hall (SRH) recombination levels having unequal capture cross sections leads to a lifetime τ, which depends on the excess carrier concentration n. This dependency can be approximated in a restricted injection range by (see e.g. [11]):

$$\tau(n) \sim n^{\alpha} \tag{1}$$

For carrier-independent lifetime $\alpha = 0$ holds, hence the lifetime is independent of the carrier density, and in the high-injection limit of a dominating SRH defect $\alpha = 1$ holds. In reality in most cases α is between 0 and 1. Then the carrier-dependence of τ is usually described by the overlapping action of two SRH defects [12]. For multicrystalline cells it has been found that this behavior is due to injection-dependent lowering of potential barriers around recombination-active GBs [13]. In "good" regions where the diffusion length L_d is larger than the cell thickness d ($L_d > d$), the saturation current density J_{01} is proportional to $1/\tau$. On the other hand, in "poor" regions with short diffusion length ($L_d < d$) and depth-homogeneous τ, J_{01} is proportional to $1/\sqrt{\tau}$ [14]. For injection-independent τ and L_d, we would have in the whole bulk ($V_{d,i}$ = local diode voltage, i = position index, V_T = thermal voltage) [7]:

$$n \sim \exp\left(\frac{V_{d,i}}{V_T}\right) \tag{2}$$

In recombination-active grain boundaries $d > L_d$ holds. In this case, again assuming depth-homogeneous τ, we obtain with (1) and (2) a dark current density of (C, C' = temporary local constants, $J'_{01,i}$ = voltage-independent local saturation current density):

$$J(V_{\mathrm{d},i}) = \frac{C}{\sqrt{\tau(n)}} \exp\left(\frac{V_{\mathrm{d},i}}{V_{\mathrm{T}}}\right) = \frac{C'}{\sqrt{\left(\exp(\frac{V_{\mathrm{d}}}{V_{\mathrm{T}}})\right)^{\alpha}}} \exp\left(\frac{V_{\mathrm{d},i}}{V_{\mathrm{T}}}\right) = \mathrm{C}' \exp\left(\frac{(1-0.5\alpha)V_{\mathrm{d},i}}{V_T}\right) = J'_{01,i} \exp\left(\frac{V_{\mathrm{d},i}}{n_1 V_T}\right) \tag{3}$$

Hence, the ideality factor n_1 of the dark current due to grain boundary recombination in the bulk is expected to depend on α in SRH theory as:

$$n_1 = \frac{1}{1-0.5\alpha}\,. \tag{4}$$

The strong approximation behind eq. (3) is that, for varying illumination intensity, the lifetime changes but is assumed to remain homogeneous within the bulk. In reality for $L_\mathrm{d} < d$ a pronounced depth profile of n establishes, leading for an injection-dependent lifetime to a depth profile of τ, which influences $J(V_\mathrm{d})$. Moreover, a GB perpendicular to the pn-junction cannot be treated correctly by a 1-dimensional model. This will lead to a slightly different dependence of n_1 from α than in (4), but the general tendency that n_1 increases with increasing α remains. Such an increased ideality factor has been found for mc-Si cells e.g. by Macdonald et al. [12].

On the other hand, the net luminescence intensity can be described by (C_i = calibration constant at position i) [6,7]:

$$\Phi_i = C_i \exp\left(\frac{V_{\mathrm{d},i}}{V_{\mathrm{T}}}\right) \tag{5}$$

According to Fuyuki [15] C_i is proportional to L_d, which, for $L_\mathrm{d} < d$ (where this proportionality is only valid, see [10]), is proportional to $\sqrt{\tau}$. This leads with (1) and (2) to (C_i' = voltage-independent calibration constant):

$$\Phi_i = C\sqrt{\tau(n)}\, \exp\left(\frac{V_{\mathrm{d},i}}{V_{\mathrm{T}}}\right) = C' \sqrt{\left(\exp\left(\frac{V_{\mathrm{d},i}}{V_{\mathrm{T}}}\right)\right)^{\alpha}} \exp\left(\frac{V_{\mathrm{d},i}}{V_{\mathrm{T}}}\right) = C'_i \exp\left(\frac{(1+0.5\alpha)V_{\mathrm{d},i}}{V_{\mathrm{T}}}\right) =$$

$$C'_i \exp\left(\frac{V_{\mathrm{d},i}}{n_{\mathrm{lum}} V_{\mathrm{T}}}\right) \tag{6}$$

Hence, in recombination-active grain boundary positions, where $L_\mathrm{d} < d$ can be expected, a recombination-dependent lifetime will lead to an apparent luminescence ideality factor of:

$$n_{\mathrm{lum}} = \frac{1}{1+0.5\alpha} \tag{7}$$

For $\alpha > 0$ this is smaller than unity, hence in these regions we expect, due to the saturation of SRH levels, that the luminescence intensity increases with increasing V_d more strongly than proportionally to $\exp(V_\mathrm{d}/V_\mathrm{T})$. This is exactly what we observe at the special grain boundaries in Fig. 1 (b). Again, for an injection-dependent lifetime, L_d is not constant but depth-dependent. Moreover, grain boundaries crossing the pn-junction cannot be treated by a 1-dimensional model, since there is significant horizontal excess carrier current to the GB. This means that

(7) does not hold exactly, but the general tendency that n_{lum} decreases with increasing injection-dependence of τ will remain.

Please note that this apparent luminescence ideality factor smaller than unity does not mean that the basic luminescence equation $\Phi = B_{rad}\, n\, p$ does not hold anymore (B_{rad} = coefficient of radiative recombination, p = hole concentration [7]). This equation still holds at any depth in the cell and for any V_d, but the depth profile of the excess carriers may flatten with increasing V_d, which leads for increasing V_d to an increased photon yield per injected electron.

3.2. Device simulation results

For explaining the phenomenon of bright GBs in PL images in more detail, we performed two-dimensional numerical device simulations using the software Sentaurus [16]. We simulate a 1 mm wide domain with one vertical grain boundary. The defects in the grain boundary are distributed within the band gap according to a defect-pool model, which was modified from amorphous to defected silicon in [13]. Because there are acceptor-like and donor-like defects, the occupancy of these defects depend on the injection conditions and, with this, so does the stored charge and the band bending. Because the bright GBs shown in Fig. 1 b) are only moderately recombination active, we reduce the defect density by a factor of 10 compared to [13] (see Fig. 5 for p-type therein). We simulated at various illumination intensities, beginning at 0.05 suns, and extracted the PL intensity (number of photons generated by radiative recombination) at open-circuit and at short-circuit conditions, yielding $N_{ph,oc}$ and $N_{ph,sc}$. The difference between these two ($N_{ph,net}$) is proportional to the net PL signal at V_{oc}, which was also evaluated in Sect. 2. The local diode voltages V_d are the local differences of the quasi Fermi levels E_F^n -E_F^p at the depth of the pn junction in the considered position. For evaluating the apparent luminescence ideality factor we use the formula:

$$n_{\mathrm{lum}} = \frac{V_{\mathrm{d}}^{(1)} - V_{\mathrm{d}}^{(2)}}{V_T ln\left(\frac{N_{\mathrm{ph,net}}^{(1)}}{N_{\mathrm{ph,net}}^{(2)}}\right)}\ , \qquad (8)$$

where the index 1 and 2 denote simulations at two different but similar illumination intensities differing from each other by a factor of 2 or less.

Figure 2 shows the resulting ideality factor of the simulated PL intensity in dependence of V_{oc}. The V_{oc} range between 548 and 631 mV corresponds to an illumination intensity between 0.05 and 2 suns. Results for two different parts of the simulation domain are shown: one around the GB, and the other in the remaining intragrain region between two GBs lying 1 mm apart from each other (note the mirroring boundary conditions in these simulations). The lower n_{lum}

at the GB is clearly reproduced. The effect of low n_{lum} can be created irrespective of bulk lifetime, dopant density etc. and these simulation parameters are therefore not listed in detail. The slight decrease of n_{lum} also for the intragrain region at high V_{oc} is due to lateral excess carrier diffusion to the grain boundary.

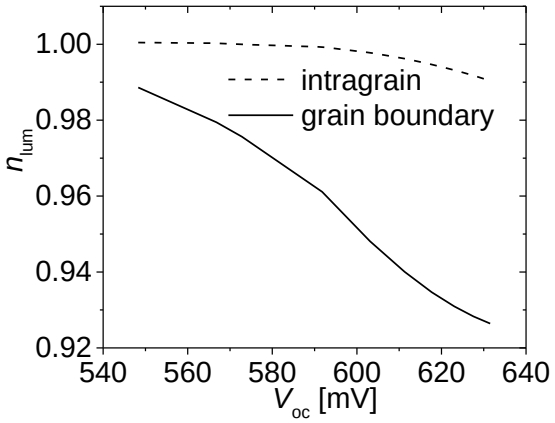

Fig. 2: Simulated apparent luminescence ideality factor as a function of V_{oc} at the grain boundary and in the intragrain region.

4. Evaluation method of the PL results

In the following a quantitative imaging of n_{lum} will be attempted. If the local diode voltage $V_{d,i}$ in any position i would be known, n_{lum} could be measured simply by measuring Φ_i at two different voltages $V_{d,i}^{(1)}$ and $V_{d,i}^{(2)}$ according to (8). Unfortunately, even at open circuit (V_{oc}) condition with an illumination intensity as low as 0.1 suns, in mc-Si cells the local diode voltages $V_{d,i}$ may differ from V_{oc} by a voltage difference $\Delta V_{d,i}$ as large as 4.7 mV [10]. For higher intensities $\Delta V_{d,i}$ becomes correspondingly larger, which becomes increasingly significant. In [3] a method was proposed, based on the linear response principle [17], for calculating $\Delta V_{d,i}$ by comparing V_{oc}-PL images $\Phi_i^{(1)}$ and $\Phi_i^{(2)}$ taken at different illumination intensities, leading to open circuit voltages $V_{oc}^{(1)}$ and $V_{oc}^{(2)}$. It has been found in [3] by evaluating numerical 2-dimensional Spice simulations of a model cell containing extended regions of increased J_{01} that the voltage response depends linearly on the illumination intensity only for very low intensities but tends to saturate already for intensities > 0.1 suns. This saturation was described in [3] by defining a non-linearity parameter X according to:

$$\Delta V_{d,i}^{(2)} = (1 + X)\Delta V_{d,i}^{(1)} \qquad (9)$$

For the considered case $I_{sc}^{(2)} = 2*I_{sc}^{(1)}$, $X = 1$ means linear response, which holds for the case evaluated in [3] only for very small intensities; as a rule there $X < 1$ holds. The value of X

depends on several parameters, such as the illumination intensity, the value of J_{01} in the defect region, the emitter sheet resistance, and also on the defect geometry and strength. Thus, the value of X holding for a certain defect region is generally unknown. In particular, not all defect regions can be assumed to show the same value of X.

Altogether we have 4 unknown variables for each position i, which are $\Delta V_{d,i}^{(1)}$, X_i, C_i', and $n_{lum,i}$. Theoretically, by measuring net V_{oc}-PL images at four different illumination intensities (e.g. at 0.1, 0.2, 0.5, and 1 sun), we should be able to obtain all these parameters for each position. Until now the parameter X was defined only for $I_{sc}^{(2)} = 2*I_{sc}^{(1)}$. For the other intensities we may define other non-linearity parameters Y and Z for $I_{sc}^{(3)} = 5\ I_{sc}^{(1)}$ and $I_{sc}^{(4)} = 10\ I_{sc}^{(1)}$, which are:

$$\Delta V_{d,i}^{(3)} = (1+Y)\Delta V_{d,i}^{(1)} \qquad \Delta V_{d,i}^{(4)} = (1+Z)\Delta V_{d,i}^{(1)} \tag{10}$$

Fortunately X, Y, and Z are not independent of each other. By evaluating all simulation points of Fig. 6 in [3] we have found that they all very accurately (maximum error 5 %) follow the relation (*suns* = illumination intensity in suns):

$$\Delta V_{d,i}(suns) = \Delta V_{d,i}^{max}\left(1 - \frac{a}{suns+a}\right) \tag{11}$$

The validity of (11) was proven also by the 2-dimensional finite element cell simulations for various illumination intensities shown below. If the two parameters a and $\Delta V_{d,i}^{max}$ in (11) are fitted to $\Delta V_i^{(1)}$ and $\Delta V_i^{(2)}$, depending on each other for a certain value of X by (9), $\Delta V_{d,i}^{(3)}$ and $\Delta V_{d,i}^{(4)}$ for 0.5 and 1 sun may be calculated by (11), leading to the values of Y and Z after (10). Combining (9) and (11) for 0.1 and 0.2 suns leads to the following expressions for the parameters a and $\Delta V_{d,i}^{max}$ as a function of X:

$$a(X) = \frac{0.2\,X}{1-X} \qquad \Delta V_{d,i}^{max} = \Delta V_{d,i}^{(1)}\frac{1+X}{1-X} \tag{12}$$

This leads with (11) for 0.5 and 1 sun to:

$$\Delta V_{d,i}^{(3)} = \Delta V_{d,i}^{(1)}\frac{1+X}{1-0.6X} \qquad \Delta V_{d,i}^{(4)} = \Delta V_{d,i}^{(1)}\frac{1+X}{1-0.8X} \tag{13}$$

This leads with (10) to:

$$Y = \frac{1.6\,X}{1-0.6\,X} \qquad Z = \frac{1.8\,X}{1-0.8\,X} \tag{14}$$

Hence, if a certain value of X is assumed, this defines Y and Z by (14). For example, for $X = 1$ (linear response) $Y = 4$ and $Z = 9$ emerges, as expected by (10).

Now we may write the expected luminescence intensities for the four net V_{oc}-PL images performed at 0.1, 0.2, 0.5, and 1 sun after (5), (8), and (9):

$$\Phi_{oc}^{(1)} = C_i'\exp\left(\frac{V_{oc}^{(1)}+\Delta V^{(1)}}{n_{lum}\,V_T}\right) \qquad \Phi_{oc}^{(2)} = C_i'\exp\left(\frac{V_{oc}^{(2)}+X\,\Delta V^{(1)}}{n_{lum}\,V_T}\right) \tag{15}$$

$$\Phi_{\mathrm{oc}}^{(3)} = C_i' \exp\left(\frac{V_{\mathrm{oc}}^{(3)} + Y\,\Delta V^{(1)}}{n_{\mathrm{lum}}\, V_{\mathrm{T}}}\right) \qquad \Phi_{\mathrm{oc}}^{(4)} = C_i' \exp\left(\frac{V_{\mathrm{oc}}^{(4)} + Z\,\Delta V^{(1)}}{n_{\mathrm{lum}}\, V_{\mathrm{T}}}\right)$$

Since Y and Z are dependent variables after (14), the independent variables in (15) are C_i', $\Delta V^{(1)}$, X, and n_{lum}. We have simulated luminescence intensities after (15) by assuming certain values for these variables and have re-extracted these variables by self-consistently solving equations (15) using the equation solver of Matlab [18]. This worked indeed, but only on simulated data without any noise. As soon as we added only 1 % statistical noise to the simulated intensities, the evaluation lead to very noisy results. Also the application of this method to experimental luminescence data did not lead to meaningful results. Note that the assumption of the validity of (11) and the assumption made in (6) that n_{lum} is independent of the diode voltage are only approximations. Therefore we consider the self-consistent solution of (15) for evaluating experimentally obtained luminescence data as not practicable. Instead, we try to obtain these variables step-by step by using the following strategy: The first step is to calculate the expected distribution of X by performing a 2-dimensional finite element device simulation of our given solar cell. In a previous paper [19] we fitted a Griddler cell model [20] to an existing inhomogeneous solar cell by evaluating DLIT and luminescence images of this cell. The DLIT results used in [19] had a spatial resolution in the order of 1 mm. Since we are interested here in a higher spatial resolution, we use in the Griddler model applied here a high-resolution J_{01} image obtained from luminescence imaging after [10]. In contrast to [19] we assume here homogeneous values of the grid and contact resistances, which lead to very similar local diode voltage results as that found in [19]. This Griddler model was then used for predicting local diode voltage images at V_{oc} for 0.1, 0.2, 0.5, and 1 sun illumination intensity. This simulation reveals $\Delta V_{\mathrm{d},i}$ data for these intensities. Fig. 3 a) shows these data for 0.1 sun intensity for the selected region of Fig. 1, the data for higher intensities look qualitatively similar. From the $\Delta V_{\mathrm{d},i}$ data for 0.1 and 0.2 suns the distribution of X shown in Fig. 3 b) is obtained after (9). We see in this distribution that in most of the area X is well-defined and close to the value of 0.86, which was obtained and used homogeneously in [3]. In these regions also the simulated data for $\Delta V_{\mathrm{d},i}$ for 0.5 and 1 sun intensity follow eq. (11) to an accuracy better than 2 %. In the strong defect regions X appears to be lower, but these regions will not be evaluated later on. In the regions where $\Delta V_{\mathrm{d},i}$ comes close to zero (red in Fig. 3 a), the obtained data for X in Fig. 3 (b) show large positive and negative values with sharp transitions. This is an artifact coming from the fact that, in contrast to our model expectation, the regions (lines) of $\Delta V_{\mathrm{d},i} = 0$ between regions of positive and negative $\Delta V_{\mathrm{d},i}$ (regions of low and high J_{01}) do not remain at exactly the

same positions for varying illumination intensity in reality. This is because of the non-linear dependence of $\Delta V_{d,i}$ on illumination intensity. Moreover, if the cell is at its global V_{oc}, due to the lateral balancing currents not all regions within the cell are at their individual V_{oc}. Therefore in these regions of low $\Delta V_{d,i}$ the prediction (9) does not hold, leading to meaningless values of X there. On the other hand, these "wrong" X data do not influence the result too much, since, if $\Delta V_{d,i}^{(1)}$ is very small, also the voltage differences for higher intensity remain small and an error in X is insignificant. Therefore, in the following evaluations we have set all values above 1 to 1 and all values below 0.5 to 0.5.

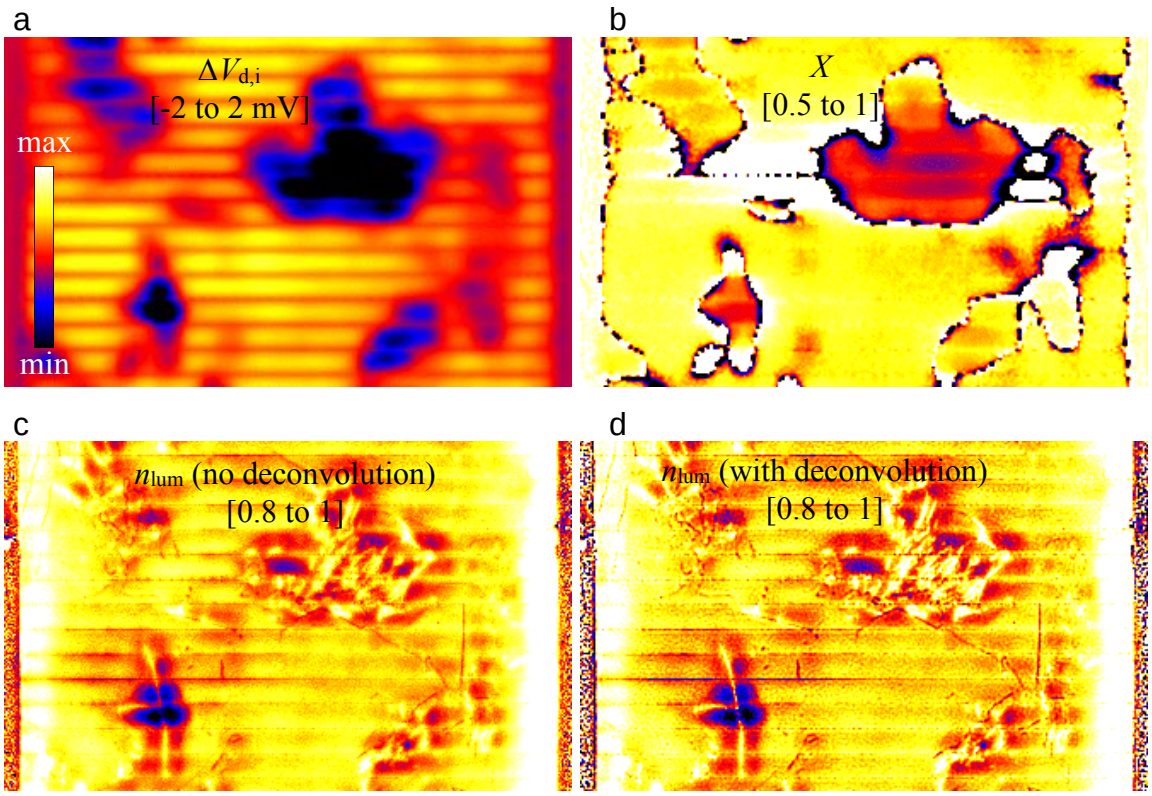

Fig. 3: a) Local voltage difference $\Delta V_{d,i}$ at 0.1 sun in the enlarged region of Fig. 1 obtained from a Griddler analysis; b) distribution of X in this region; c) distribution of n_{lum} in this region without image deconvolution; d) distribution of n_{lum} in this region after applying image deconvolution to the luminescence images.

In the next step n_{lum} and C_i are determined simultaneously by a fit of the luminescence data between 0.1 and 1 sun intensity. With the known values of $\Delta V_{d,i}^{(1)}$ and X each nominator of the exponential terms in (15), which is the local diode voltage V_d, can be calculated with Y and Z obtained after (14). Applying a linear fit to the logarithmic luminescence signal Φ_{oc} of all four net V_{oc}-PL images over their corresponding local diode voltage V_d leads to a linear function with the slope $1/(n_{lum}V_T)$ and the offset $\ln(C_i')$, see also (8). Figs. 3 c) and d) show the

determined n_{lum} without and including image deconvolution after [9] applied to the luminescence images, respectively. As it was discussed already in [10], this correction only leads to a sharpening of dark lines, which, however, is necessary here for improving the accuracy of the results for a single grain boundary. We see that in most of the area outside of the defect regions n_{lum} is lying homogeneously between 0.94 and 0.95. At the special grain boundaries, which appeared bright in the ratio image in Fig. 1 b), the value of n_{lum} in Fig. 3 d), which is based on the deconvoluted luminescence images considered to be more correct, reduces down to a value of 0.89. In the defect regions n_{lum} is strongly fluctuating. We assume that this is also an artifact coming from the fact that our approximation (11) for describing the non-linearity of the voltage difference to V_{oc} does not hold anymore in regions of strongly fluctuating J_{01}. Hence, we believe that in these defect regions the PL evaluation method described in this Section is not applicable. The same holds for the regions close to the busbars, which appear to show $n_{lum} > 1$. Here we are at the border between illuminated and shadowed regions, where eq. (11) also does not hold anymore.

5. ReBEL, SEM, TEM, and hyperspectral PL imaging results

For obtaining more information on the physical nature of the special GBs showing intensity-dependent recombination and of other GBs not showing this effect, reverse-bias electroluminescence (ReBEL [4]), scanning electron microscopy (SEM), transmission electron microscopy (TEM) and hyperspectral PL imaging [5] has been applied, the latter to another cell region in a parallel wafer showing similar grain boundaries. It was shown in [4] and also in [21] that defect-induced (type-2) breakdown occurs predominantly at strongly recombination-active GBs. This breakdown is caused by iron silicide needles [22], and the recombination activity of these GBs is most probably due to iron contamination. Fig. 4 a) shows a superposition image of the V_{oc}-PL image of the detail in Fig. 1 a) in grey with the ReBEL image of this region at -14 V in red. This image shows that the special GB showing injection-dependent recombination (arrow *b*) shows no or only a few breakdown sites, as does a GB showing no injection-dependent recombination (arrow *a*). As found already in [21], also here most breakdown sites are found in the GB clusters.

The SEM image of GB *a* at the top of Fig. 4 b) shows that this GB is only weakly attacked by the texturing etch, whereas GB b in Fig. 3 c) is strongly attacked. The TEM image of GB *a* in the bottom of Fig. 3 b) was taken in [110] viewing direction on a Philips CM 20T electron microscope. The GB is lying somewhat inclined to the surface normal. The selected area diffraction pattern in the inset shows that this is a small angle GB with a tilt of approximately

1.7°. GB *b* in Fig. 4 c), on the other hand, is a large angle GB. The high-resolution TEM (HRTEM) image in Fig. 4 c) was taken at a FEI TITAN 80-300 microscope. Also here the GB is inclined to the surface. Here only the upper grain could be oriented to [110] but not the lower one. Separate diffraction patterns obtained on both grains yielded a relative grain misorientation angle of about 29.7°.

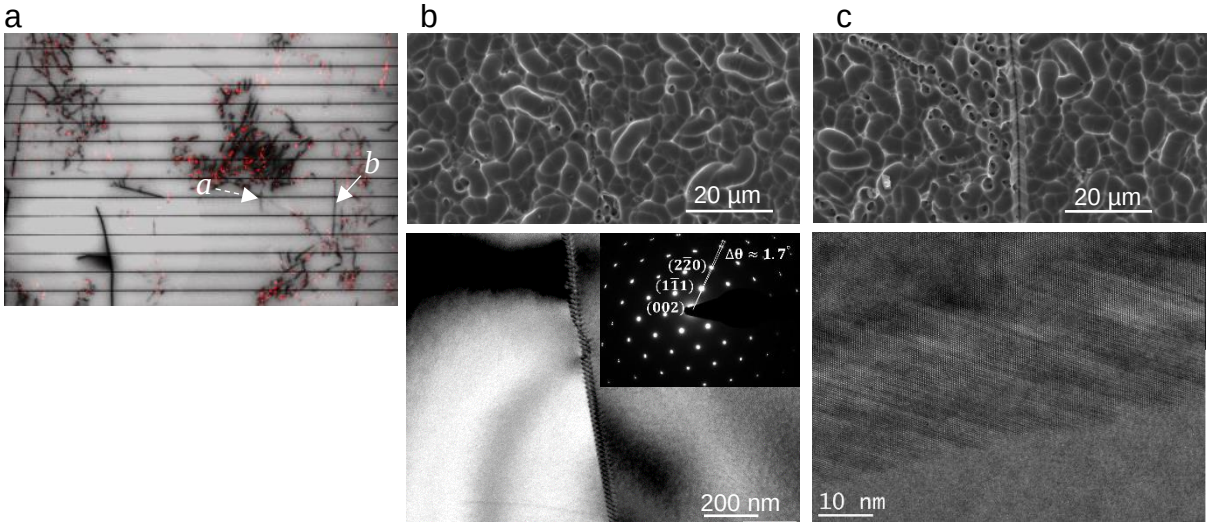

Fig. 4 a) superposition of V_{oc}-PL (grey) and ReBEL image (red) of the detail region shown in Fig. 1; b) SEM (top) and TEM micrograph (bottom) of position *a*, inset: selected area electron diffraction pattern; c) SEM (top) and HRTEM micrograph (bottom) of position *b*.

Hyperspectral photoluminescence imaging provides a near infrared spectrum for each pixel in the recorded image, and has been performed to get information of the spatial distribution of different types of radiative defects [5,23,24]. Local low-temperature luminescence emission spectra of different grain boundaries have already been published by Tajima et al. [25]. Hyperspectral PL images were obtained by using a NIR hyperspectral pushbroom camera (SWIR, Specim, Finland). The HgCdTe detector has a spectral sensitivity in the 929–2531 nm (0.49–1.33 eV) range with a resolution of 6 nm (256 bands). The spatial resolution in this study was 27 and 116 µm. As excitation source, an 808 nm line laser was used with an irradiated power density of approximately 2 W/cm^2 (Lasiris Magnum II). To prevent laser beam reflections from entering the camera's optics, a 1000 nm low-pass filter was used. The sample was cooled to 90 K on a polished aluminum surface on top of a cryogenic cooler filled with liquid nitrogen.

To separate the different radiative defects, a multivariate curve resolution analysis (MCR) was carried out [26]. MCR is a mathematical method in multivariate statistics for deconvoluting

complex, convoluted signals composed of several discrete, simultaneously occurring signals and can be represented mathematically by Eq. (15):

$$D = CS^T + E \tag{15}$$

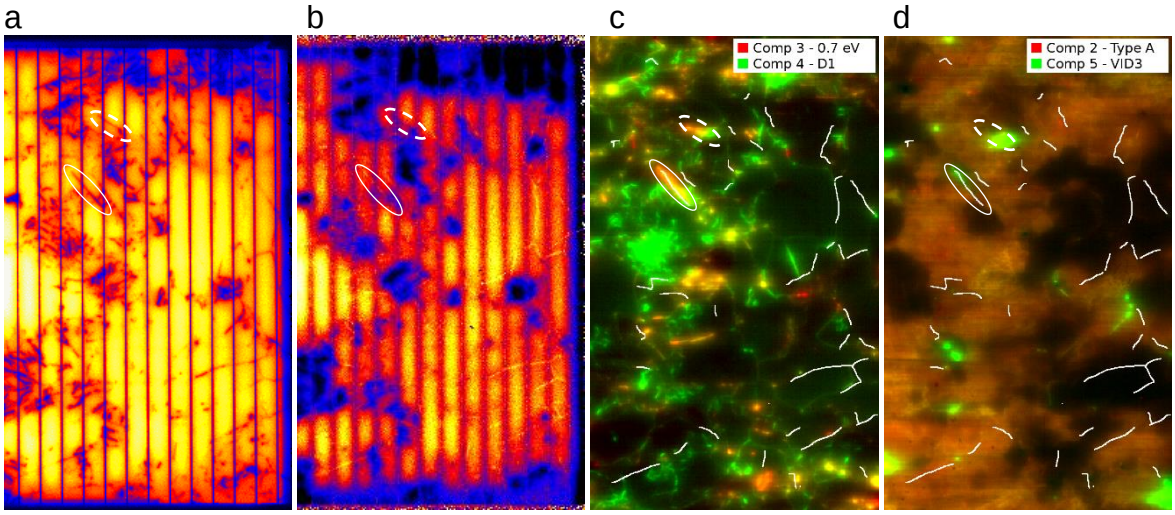

Fig. 5: a) V_{oc}-PL image (1 sun) of a region in the second investigated cell; b) ratio of V_{oc}-PL images at 1 and at 0.1 suns intensity; c) hyperspectral PL image of component 3 and 4, obtained from MCR analysis (red: component 3 with center peak energy 0.7 eV, green: component 4 at 0.82 eV (D1)); d) hyperspectral PL image (red: component 2 – two peaks, 0.94 and 1.00 eV (Type A), green: component 5 at 0.93 eV (VID3)). In areas where two components are present, the colors blend.

In MCR, the measured data, matrix D, are decomposed into a number of representative scores in matrix S^T, with corresponding loading vectors in C. An error matrix, E, represents the difference between the recorded and the simulated signal. An alternating least squares (ALS) algorithm is used to minimize E. The different radiative defects are manifested as different components, with images of the spatial distribution of each defect in S^T and their corresponding spectrum in C. The MCR algorithm in PLS_Toolbox version R8.2.1 (Eigenvector Research, Inc., USA) running on MATLAB R2016b (The MathWorks, Inc., USA) was used in this study.

The hyperspectral investigations were made on a passivated wafer, which is a neighboring wafer of the second investigated cell produced by the same technology as the first one. Fig. 5 a) shows a V_{oc}-PL image of a typical region in this second cell and (b) shows the ratio image using V_{oc}-PL images at 1 and 0.1 suns, respectively. Again, in the ratio image some special grain boundaries show up as bright lines, one of them is indicated as a white ellipse. Another grain boundary, which does not appear bright in Fig. 5 b), is marked as a dashed ellipse. In Fig.

5 c) and d) the positions of the special GBs showing injection-dependent recombination are marked as white lines.

The hyperspectral analysis of the neighboring wafer of this region revealed 5 spectral components between 0.49 and 1.3 eV photon energy. Fig. 5 c) and d) show the distribution of 4 of these components in this region. Component 1 is the band-to-band PL, not shown here, but the spatial distribution is anti-correlated with component 2's, i.e., band-to-band PL in the dark areas of Fig. 5 d). Component 2 is identified as Type A defect, cf. [27], areas where the component's PL spectrum has peaks at 0.94 eV (D3) and at 1.00 eV (D4). The white lines show no correlation with neither band-to-band PL nor Type A defects, since the white lines are distributed approximately evenly between them. Component 3, 4 and 5 can be tentatively identified as interstitial iron, Fe_i, cf. [28], a Type B defect (D1), cf. [27] and VID3 of unknown origin, cf. [29], respectively. None of the special GBs, except of the one marked by the ellipse denoted with a solid white line, shows any significant defect luminescence. The marked GB shows luminescence of components 3, 4 and 5. A close-up image of the spatial distribution and respective spectra of these components, is shown in Fig. 6. The analysis shows that there are three spectral components (comp 3, 4, and 5) present in the GB. However, in spite of the relatively homogeneous appearing recombination strength of the GB visible in Fig. 5 (a), the distribution of the different luminescence components is very inhomogeneous.

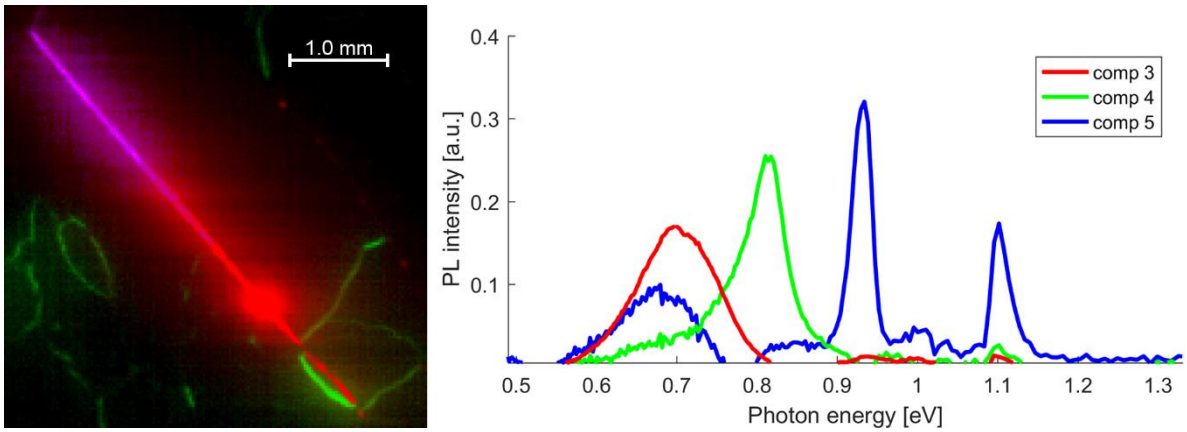

Fig. 6: Spatial distribution and respective spectra of components obtained from MCR analysis of PL from the GB marked by a solid white ellipse in Fig. 5. Each component has its own color, but in areas where two or more are present, the colors blend.

6. Discussion and conclusions

In this contribution evidence has been presented that, in certain special grain boundaries, the recombination is significantly injection intensity-dependent. This can easily be proven by displaying the ratio of V_{oc}-PL images taken at different illumination intensities. In these images

these special GBs show up as bright lines, whereas other GBs and GB clusters do not or show up as dark areas. This injection dependence leads, if the recombination activity is high enough, to an apparent ideality factor of the luminescence smaller than unity. We attempted to measure this ideality factor by evaluating V_{oc}-PL images taken at various illumination intensities and regarding the influence of horizontal balancing currents by applying and further developing a recently proposed non-linear response description of this effect. However, this description is only approximate and does not hold in the whole cell area. Nevertheless luminescence ideality factors of 0.95 in undisturbed regions and 0.89 in the special GBs have been found. These values are in the same order as that revealed by a Sentaurus simulation of a domain in a cell containing a GB. An accurate theory relating this luminescence ideality factor of GBs to corresponding recombination ideality factors larger than 1 is still missing.

Other physical investigations of these special GBs have not revealed any particularities. TEM analysis has shown that at least one of them is a large angle GB, whereas a nearby lying GB not showing this injection dependence is a small angle GB. The special GBs do not contain particular defect-induced breakdown sites, and, with only one exception, they do not show significant defect luminescence. Hyperspectral PL investigation of the one GB showing defect luminescence has revealed an inhomogeneous distribution of three different luminescence components. This leads us to the conclusion that these GBs are relatively clean ones, hence they obviously show a moderate density of deep level defects. Such deep level defects in high numbers should lead to defect luminescence, and they would tend to pin the Fermi level for the depletion regions around the defects. If the density of such deep levels is low, however, the trapped charge and a possible potential barrier around the GBs reduce with increasing injection intensity (electron concentration) and the recombination activity gradually reduces. We believe that this is the mechanism responsible for the observed injection-dependent recombination of these special GBs. This interpretation is supported by the Sentaurus simulations, which have revealed that the apparent luminescence ideality factor smaller than unity only appears if the density of states at the GB is moderate. It would be very interesting to compare our results with nano-XRF studies as performed e.g. by Bernardini et al. [30].

These results are a contribution to a deeper understanding of the electronic behavior of GBs in mc solar silicon material. As usual, the results raise more questions than they answer. Thus, the connection between an observed luminescence ideality factor smaller than 1 to a recombination ideality factor larger than 1 for a GB going into the depth of the material still has to be established. Also the method for measuring (imaging) the luminescence ideality factor under the influence of horizontal balancing currents still has to be improved. Generally,

understanding the connection between spectral defect luminescence and the electronic properties of GBs and other defects is still at its beginning.

Acknowledgements

The authors would like to thank for the financial support by the German Federal Ministry for Economic Affairs and Energy and by industry partners within the research cluster "SolarLIFE" (contract no. 0325763 D). T. Mehl's work has been a part of the FME-SuSolTech research centre financed by The Research Council of Norway. The content is in the responsibility of the authors.

References

[1] J. Chen. B. Chen, T. Sekiguchi, M. Fukuzawa, and M. Yamada, Correlation between residual strain and electrically active grain boundaries in multicrystalline silicon, Appl. Phys. Lett. 93 (2008) 112105.
[2] J. Bauer, A. Hähnel, P. Werner, N. Zakharov, H. Blumtritt, A. Zuschlag, and O. Breitenstein, Recombination at Lomer dislocations in multicrystalline silicon for solar cells, IEEE Journal of Photovoltaics 6 (2016) 100-110.
[3] O. Breitenstein, J. Bauer, D. Hinken, and K. Bothe, Towards an improved Laplacian-based photoluminescence image evaluation method, Solar En. Mat. & Solar Cells 142 (2015) 92-101.
[4] D. Lausch, K. Petter, H. v. Wenckstern, and M. Grundmann, Correlation of pre-breakdown sites and bulk defects in multicrystalline silicon solar cells, Phys. Status Solidi RRL 3 (2009) 70-72.
[5] I. Burud, A.S. Flø, and E. Olsen, On the origin of inter band gap radiative emission in crystalline silicon, AIP Advances 2 (2012) 042135.
[6] T. Trupke, E. Pink, R.A. Bardos, and M.D. Abbott, Spatially resolved series resistance of silicon solar cells obtained from luminescence imaging, Appl. Phys. Lett. 90 (2007) 093506.
[7] K. Bothe and D. Hinken, Quantitative Luminescence Characterization of Crystalline Silicon Solar Cells, in "Advances in Photovoltaics, Volume 2" (ed. G.P. Willeke and E.R. Weber), Academic Press (Burlington), Elsevier (2013).
[8] D. Walter, A. Fell, E. Franklin, D. MacDonald, B. Mitchell, and T. Trupke, The impact of silicon CCD photon spread on quantitative analyses of luminescence images, IEEE Journal of Photovoltaics 4 (2014) 368-373.
[9] O. Breitenstein, F. Frühauf, and A. Teal, An improved method to measure the point spread function of cameras used for electro- and photoluminescence imaging of silicon solar cells, IEEE Journal of Photovoltaics 6 (2016) 522-527.
[10] O. Breitenstein, F. Frühauf, D. Hinken, and K. Bothe, Effective diffusion length and bulk saturation current density imaging in solar cells by spectrally filtered luminescence imaging, IEEE Journal of Photovoltaics 6 (2016) 1243-1254.
[11] O. Breitenstein, F. Frühauf, J. Bauer, F. Schindler, and B. Michl, Local solar cell efficiency analysis performed by injection-dependent PL imaging (ELBA) and voltage-dependent lock-in thermography (Local I-V), Energy Procedia 92 (2016) 10-15.
[12] D. Macdonald and A. Cuevas, Reduced fill factors in multicrystalline silicon solar cells due to injection-level dependent bulk recombination lifetimes, Prog. Photovolt: Res. Appl. 8 (2000) 363-375.
[13] P.P. Altermatt and G. Heiser, Predicted electronic properties of polycrystalline silicon from three-dimensional device modeling combined with defect-pool model, J. Appl. Phys. 92, No. 2 (2001) 2561-2574.
[14] O. Breitenstein, The physics of industrial crystalline silicon solar cells, in "Advances in Photovoltaics, Volume 2" (ed. G.P. Willeke and E.R. Weber), Academic Press (Burlington), Elsevier (2013).
[15] T. Fuyuki, H. Kondo, T. Yamazaki, Y. Kaji, A. Ogane, and Y. Takahashi, Analytic findings in the electroluminescence characterization of crystalline silicon solar cells, *J. Appl. Phys.*, vol. 101, art. no. 023711, 2007.
[16] Synopsys Inc. (Mountain View, CA, USA).
[17] J.-M. Wagner, A. Schütt, J. Carstensen, and R. Adelung, Linear-response description of the series resistance of large-area silicon cells: Resolving the difference between dark and illuminated behavior, Energy Procedia 92 (2016) 255-264.

[18] see http://de.mathworks.com/products/matlab/index.html?requestedDomain=uk.mathworks.com (Jan. 2017).
[19] F. Frühauf, J. Wong, J. Bauer, and O. Breitenstein, Finite element simulation of inhomogeneous solar cells based on lock-in thermography and luminescence imaging, Sol. Energy Mat. Sol. Cells 162 (2017) 103-113.
[20] J. Wong, Griddler: Intelligent computer aided design of complex solar cells, Proc. 40th IEEE PVSC, Tampa 2013, pp. 933-938.
[21] O. Breitenstein, J. Bauer, K. Bothe, W. Kwapil, D. Lausch, U. Rau, J. Schmidt, M. Schneemann, M.C. Schubert, J.-M. Wagner, and W. Warta, Understanding junction breakdown in multicrystalline solar cells, J. Appl. Phys. 109 (2011) 071101.
[22] A. Hähnel, J. Bauer, H. Blumtritt, O. Breitenstein, D. Lausch, W. Kwapil, Electron microscope verification of breakdown-inducing α-$FeSi_2$ needles in multicrystalline silicon solar cells, J. Appl. Phys. 113, 044505 (2013).
[23] E. Olsen and A.S. Flø, Spectrally and spatially resolved imaging of photoluminescence in multicrystalline silicon wafers, Appl. Phys. Lett. 99 (2011), 011903.
[24] I. Burud, T. Mehl, A. Flo, D. Lausch and E. Olsen, Hyperspectral photoluminescence imaging of defects in solar cells, J. Spectral Imaging 5 (2016) a8.
[25] M. Tajima, Y. Iwata, F. Okayama, H. Toyota, H. Onodera, and T. Sekiguchi, J. Appl. Phys. 111 (2012) 113523.
[26] R. Tauler, Multivariate curve resolution applied to second order data, Chemometr. Intell. Lab. Syst. 30 (1995) 133–146.
[27] D. Lausch, T. Mehl, K. Petter, AS. Flø, I. Burud, and E. Olsen, Classification of crystal defects in multicrystalline silicon solar cells and wafer using spectrally and spatially resolved photoluminescence, J. Appl. Phys. 119 (2016) 054501.
[28] T. Mehl, M. Di Sabatino, K. Adamczyk, I. Burud and E. Olsen. Defects in multicrystalline Si wafers studied by spectral photoluminescence imaging, combined with EBSD and dislocation mapping, Energy Procedia 92 (2016) 130-137.
[29] A. Flø, I. Burud, K. Kvaal, R. Søndenå, and E. Olsen, Distribution of radiative crystal imperfections through a silicon ingot, AIP Advances 3 (2013) 112120.
[30] S. Bernardini, Nano-XRF analysis of metal impurities distribution at PL active grain boundaries during mc-silicon solar cell processing, IEEE J. Photovolt. 7 (2017) 244-249.